


## Article

# Study of Water–Sand Inrush through a Vertical Karst Conduit Uncovered through Tunnel Excavation

Zhenhua Zhao <sup>1,2</sup>, Hailong Wang <sup>1,2,3,4,\*</sup> , Lin Han <sup>1,2</sup> and Zhenlong Zhao <sup>3</sup>

<sup>1</sup> No.801 Hydrogeology and Engineering Geological Brigade of Shandong Provincial Bureau of Geology and Mineral Resources, Jinan 250014, China

<sup>2</sup> Shandong Engineering Research Center for Environmental Protection and Remediation on Groundwater, Jinan 250014, China

<sup>3</sup> School of Civil Engineering and Architecture, Linyi University, Linyi 276000, China

<sup>4</sup> State Key Laboratory for Geomechanics and Deep Underground Engineering, China University of Mining and Technology-Beijing, Beijing 100083, China

\* Correspondence: whlmlp@163.com

**Abstract:** The existence of karst compromises the safety of underground engineering, especially during tunnel excavations. Karst conduits are uncovered through tunnel excavations, which may lead to a water–sand inrush disaster. Taking a vertical karst conduit as an example, the process of water–sand inrush through a karst conduit could be viewed as being similar to the process whereby a water–sand mixture flows through the discharge opening of a storage bin. In this study, based on force analysis of a non-aqueous sand body above a karst conduit, the limiting diameter of the karst conduit under force equilibrium was obtained. Considering the effect of water on aqueous sand bodies, the criterion of water–sand inrush was established. We aimed to study water–sand migration and inrush through vertical karst conduits in order to obtain the distribution of the water pressure near a vertical karst conduit, and to explore the relationship between the conduit size, water pressure, and water–sand flow rate; therefore, a simulated testing system for analyzing water–sand inrush through a vertical karst conduit was developed. When the water pressure in the testing chamber was close to the critical head pressure of the water–sand inrush, the water–sand inrush exhibited a pattern of instability—migration—deposition—stability. When the water pressure in the testing chamber exceeded the critical head pressure, the water–sand flow increased first and then stabilized over time. With the increase in the set values of the water pressure and conduit size, the steady flow of the water–sand mixture increased gradually. When the karst conduit was opened suddenly, the actual water pressure in the testing chamber decreased significantly, due to the water–sand mixture flowing out of the testing chamber and the water supply lagging behind. With the stabilization of the water–sand flow, the actual water pressure gradually tended towards stability, but it was still lower than the initial set water pressure. When the karst conduit was opened, the values of the water pressure monitored by the pore pressure gauges all clearly decreased. With the stabilization of the water–sand flow, the water pressure gradually became stable. With the increase in the distance between the pore pressure sensor and the karst conduit, the water pressure values all increased gradually. These test results are significant for further studies of the formation mechanisms of water–sand inrush through vertical karst conduits.

**Keywords:** water–sand inrush; vertical karst conduit; tunnel excavation; water–sand flow; distribution of water pressure



**Citation:** Zhao, Z.; Wang, H.; Han, L.; Zhao, Z. Study of Water–Sand Inrush through a Vertical Karst Conduit Uncovered through Tunnel Excavation. *Water* **2023**, *15*, 2010. <https://doi.org/10.3390/w15112010>

Academic Editor: Roberto Greco

Received: 6 March 2023

Revised: 11 May 2023

Accepted: 23 May 2023

Published: 25 May 2023



**Copyright:** © 2023 by the authors. Licensee MDPI, Basel, Switzerland. This article is an open access article distributed under the terms and conditions of the Creative Commons Attribution (CC BY) license (<https://creativecommons.org/licenses/by/4.0/>).

## 1. Introduction

As the product of corrosion and erosion, karst varies in terms of its development, size, and shape [1–3]. Globally, the distribution area of karst is  $22 \times 10^6$  km<sup>2</sup>, which is 15% of the world's total land area. Karst is also widely distributed throughout China [4–7]; here, the distribution area of karst is  $3.44 \times 10^6$  km<sup>2</sup> or 35.8% of the total land area [8]. Engineering

construction in karst areas presents unavoidable problems [9–12]. The existence of karst threatens the construction safety of underground engineering, especially the excavation of tunnels [13–15]. Karst conduits are uncovered through tunnel excavation, which may lead to a water–sand inrush disaster [16,17]. The filling material in karst conduits generally has the characteristics of a loose structure, large pores, and high permeability [18]. With continuous excavation, when the tunnel excavation face is close to the karst conduit, the filling material in the karst conduit will flow away quickly under the water pressure [19]. Because the karst conduit is no longer filled with filling material, the water–sand mixture in the karst cavity will easily flow into the tunnel through the karst conduit, which may lead to property losses and even casualties and seriously threatens the safety of the tunnel excavation [20,21]. In order to overcome the serious problems of water–sand inrush through karst conduits uncovered through tunnel excavation, studies of water–sand migration and inrush through karst conduits are urgently needed [22–25].

Much research has been conducted regarding the issue of water–sand migration and inrush through karst conduits. Zhou et al. [26] and Pan et al. [27] developed a visual 3D fluid–solid coupled testing platform to simulate water–sand inrush through a filled karst conduit. The evolution process of water–sand inrush can be divided into the following phases: the formation, extension, and connection of fissures, and finally the occurrence of water inrush. Wang et al. [28] developed a test system for water–sand inrush in order to study water–sand migration and inrush. The water–sand stationary flow tends to increase with the increase in water pressure. Zhou et al. [29] carried out a large-scale 3D model test on water inrush in filled-type karst conduits. The process of water inrush was accurately reproduced, and the catastrophic characteristics of water inrush in filled-type karst conduits were revealed. Chu [30] established three types of filled karst pipe mechanical instability models and obtained the corresponding criteria. The mechanism and whole evolution process of karst conduit water bursting are reflected. Huang et al. [31] built a conceptual model of water inrush induced by fracture connections. Groundwater mainly flows through the main seepage conduit rather than the impermeable area, resulting in concentrated water-inrush points. In a theoretical analysis, Li et al. [32] explored the effects of water–rock interaction mechanisms on water outbursts and the projection of mud and soil during the construction of karst tunnels. Using numerical simulation, Liu et al. [33] found that the bursting of karst water in tunnels is a gradual process that is influenced by the water pressure, different filling materials, and the plastic zones around the tunnel.

Because this type of excavation engineering takes place underground, the mechanisms and influencing factors of water–sand inrush through karst conduits are difficult to obtain through field measurements; therefore, laboratory tests are the most effective means of solving these issues [34,35]. Previous studies were mainly conducted with laboratory tests, which have provided us with a good understanding of the mechanisms and influencing factors of water–sand inrush through karst conduits, but the existing testing systems still have some deficiencies. (1) Once the phenomenon of water–sand inrush occurs, the water pressure in the testing chamber will decrease rapidly until it disappears, which is only applicable to low-volume karst or that with non-continuous recharge. For large volumes of karst or that with continuous recharge, there is a certain decrease in the water pressure in the karst during the initial stage of water–sand inrush, but then it will gradually approach a dynamic stable value. (2) Different head pressures are usually obtained by adjusting the height of the water tank or the water level in the water tank, but only the lower head pressure can be obtained due to the limited testing space. (3) The distribution of the water pressure near the karst conduit cannot be monitored during water–sand inrush. In order to study water–sand migration and inrush through a karst conduit, we obtained the distribution of the water pressure near the karst conduit and then explored the relationship between the conduit size, water pressure, and water–sand flow rate. Taking a vertical karst conduit as an example, based on an analysis of the occurrence mechanisms of water–sand inrush, a simulated testing system for water–sand inrush through vertical karst conduits

was developed. The research results are significant for further studies of the formation mechanisms of water–sand inrush through vertical karst conduits.

## 2. Occurrence Mechanism of Water–Sand Inrush through Vertical Conduits

A vertical karst conduit could be viewed as being akin to the discharge opening of a storage bin; therefore, water–sand inrush through a karst conduit constitutes the process of a water–sand mixture flowing through the discharge opening of a storage bin. One point (“m”) near the karst conduit was selected as the object of study, hereafter referred to as point m. The stress state of point m can be expressed in a polar stress diagram, as shown in Figure 1a. When the karst conduit is uncovered, that is, the gate of the discharge opening is opened, the stress state of point m will change accordingly, as shown in Figure 1b. In the initial stage, the vertical pressure ( $\sigma_{1,0}$ ) begins to decrease, and the deformation of the sand grain is elastic. After that, the vertical pressure becomes lower than the horizontal pressure, and plastic deformation occurs in the non-aqueous sand body. At a certain point, the non-aqueous sand body will appear in an arched condition, and the vertical pressure becomes zero. Since vertical planes ( $n_1 - n_2$ ) and ( $n_3 - n_4$ ) are symmetric and their stress states are exactly the same, only vertical plane ( $n_1 - n_2$ ) was analyzed. Due to the flow of the water–sand mixture, shear stress will be generated in vertical plane ( $n_1 - n_2$ ), meaning that, on vertical plane ( $n_1 - n_2$ ), the polar axis of each point will be tilted by an angle ( $\varphi$ ). If the vertical shear force acting around the entire karst conduit is sufficient to support the weight of the non-aqueous sand body located above the conduit, the sand body above the karst conduit will form an arch, and its contour will coincide with the maximum principal stress path line ( $n_1on_4$ ), as shown in Figure 1b. The arch line belongs to the range of the free surface of the non-aqueous sand body, and thus the normal stress along its whole length is 0. The arch model of the karst conduit is shown in Figure 1c. Unit (1234), formed by vertical planes (1–2) and (3–4) and surfaces (1–4) and (2–3), as described by the principal stress path line, was taken as the research object; the unit thickness is in a direction perpendicular to the page. The resultant stress ( $\sigma$ ) acting on vertical planes (1–2) and (3–4) is decomposed into normal stress ( $\sigma_b$ ) and shear stress ( $\tau_b$ ). The gravity force of unit (1234) is given by

$$G = d\Delta h\rho g \quad (1)$$

where  $G$  is the gravity force of unit (1234),  $d$  is the diameter of the karst conduit,  $\Delta h$  is the height of unit (1234),  $\rho$  is the density of the non-aqueous sand body, and  $g$  is the gravitational acceleration.

When the arch structure of the non-aqueous sand body reaches force equilibrium, its equilibrium condition is given by

$$G = 2\Delta h\tau_b \quad (2)$$

Combining Formulas (1) and (2), the shear stress ( $\tau_b$ ) is given by

$$\tau_b = \frac{d\rho g}{2} \quad (3)$$

The initial shear stress ( $\tau_0$ ) is given by

$$\tau_0 = \frac{\tau_b}{1 + \sin \varphi} \quad (4)$$

The limit diameter ( $d_{\text{lim}}$ ) of the karst conduit under force equilibrium is given by

$$d_{\text{lim}} = \frac{2\tau_0(1 + \sin \varphi)}{\rho g} \quad (5)$$

where  $d_{\text{lim}}$  is the limit diameter of the karst conduit, and  $\varphi$  is the internal friction angle.

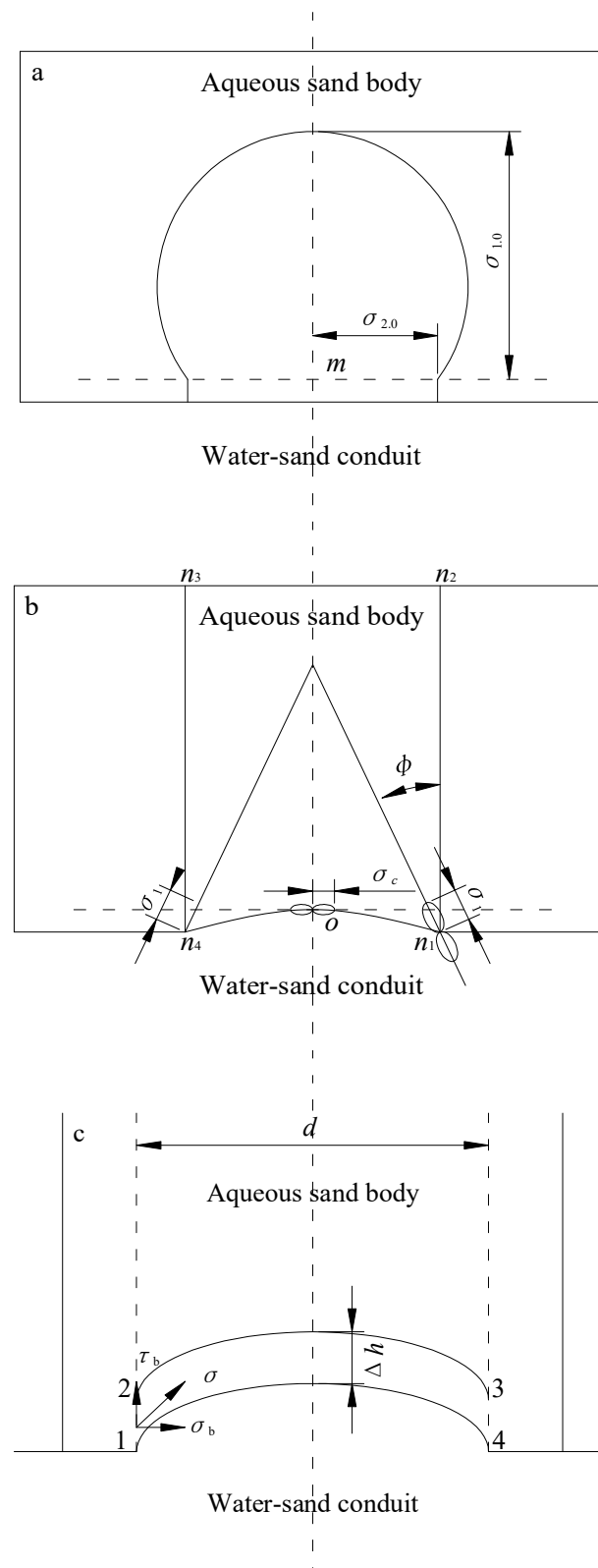


**Figure 1.** Force analysis of the non-aqueous sand body above the karst conduit: (a) polar stress diagram; (b) stress state of point  $m$ ; (c) arch model of the karst conduit.

Under the action of water, in addition to their own gravity and the cohesive force between them, the sand particles are also affected by drag force, osmotic pressure, and friction between the sand particles.

The gravity of the aqueous sand body under water is given by

$$W = \frac{1}{2}(\gamma_s h_s - \gamma h)d \quad (6)$$

where  $h_s$  is the vertical distance from the karst conduit to the surface,  $\gamma_s$  is the unit weight of the water body, and  $h$  is the thickness of the aquifer.

During water–sand inrush, the flow velocity at the top of the sand grain is lower than that at the bottom, but the flow pressure is higher than that at the bottom. The difference in pressure between the top and bottom of the sand grain creates a downward drag force on the sand grain, which is given by

$$F_L = C_L d \frac{\gamma v_0^2}{2g} \quad (7)$$

where  $C_L$  is the lifting force coefficient, which is related to the flow pattern around the sand grain and the method of determining the water velocity.

In addition, due to the loss and recharge of water in the aqueous sand body, the vertical seepage velocity is given by

$$v_s = K J_s \quad (8)$$

where  $K$  is the permeability coefficient of the aqueous sand body, and  $J_s$  is the vertical hydraulic gradient.

The osmotic pressure of the sand body is given by

$$F_s = C(1 + e)\gamma d J_s \quad (9)$$

where  $e$  is the porosity of the aqueous sand body, and  $J_s$  is the coefficient, which is 0.35~0.50.

There is a bonding force between the fine sand particles, which is proportional to the particle size and is given by

$$N = \xi D \quad (10)$$

where  $\xi$  is the coefficient, which is related to the surface properties of the sand grains and the contact compactness between them.

Because the particle size of the aqueous sand body is very small, the bonding force is relatively small during water–sand inrush, so it can be ignored.

Frictional resistance between the sand grains is given by

$$F_f = \frac{1}{2}\mu(\gamma_s h_s - \gamma h)d \quad (11)$$

where  $\mu$  is the friction coefficient between the sand grains.

Considering the effect of water on the aqueous sand body, and assuming that  $\Delta h$  is the unit height (that is,  $\Delta h = 1$ ), when the arch structure of the aqueous sand body reaches force equilibrium, its equilibrium condition is given by

$$W + F_L + F_s = F_f + \tau_b \Rightarrow \tau_b = W + F_L + F_s - F_f \quad (12)$$

Placing Equations (6), (7), (9), and (11) into Equation (12) produces

$$\tau_b = \frac{1}{2}(\gamma_s h_s - \gamma h)d + C_L d \frac{\gamma v_0^2}{2g} + C(1 + e)\gamma d J_s - \frac{1}{2}\mu(\gamma_s h_s - \gamma h)d \quad (13)$$

Considering the effect of water on the aqueous sand body, the limit diameter ( $d_{lim}$ ) of a karst conduit under force equilibrium is given by

$$d = \frac{2\tau_0(1 + \sin \varphi)}{(1 - \mu)(\gamma_s h_s - \gamma h) + C_L \frac{\gamma v_0^2}{g} + 2C(1 + e)\gamma J_s} \quad (14)$$

Therefore, the criterion of water–sand inrush is given by

$$d > \frac{2\tau_0(1 + \sin \varphi)}{(1 - \mu)(\gamma_s h_s - \gamma h) + C_L \frac{\gamma v_0^2}{g} + 2C(1 + e)\gamma J_s} \quad (15)$$

### 3. Testing System and Scheme

#### 3.1. Testing System

The simulated testing system for water–sand inrush through a karst conduit consists of a loading support bracket, a confined water chamber (loading head), a testing chamber, the base of the testing chamber, a storage tank, a servo control system for the water pressure and water yield, a servo control system for displacement and stress, and a console, as shown in Figure 2.

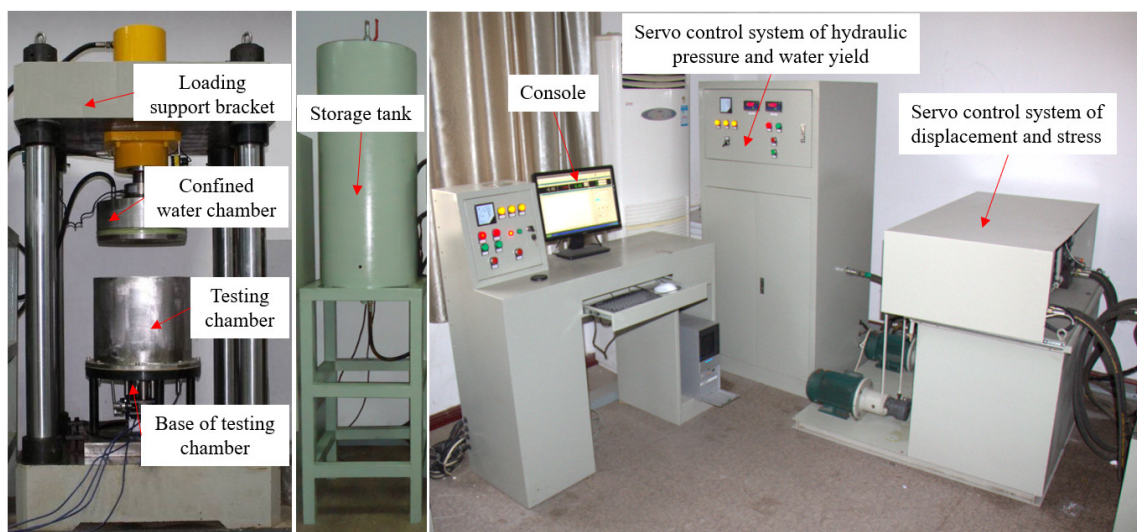


**Figure 2.** Simulated testing system for water–sand inrush through a karst conduit.

#### (1) Loading support bracket

According to the structure of the testing chamber, the loading support bracket consists of a base, a frame, a fixing device for the hydraulic cylinder, and a column. Four columns are fixed on the base, which provide a constraint reaction force when the loading head imposes a vertical load on the sample. The hydraulic cylinder is fixed on the beam, which is firmly supported by the four columns.

#### (2) Confined water chamber

The confined water chamber can supply water to the testing chamber, which is connected to the hydraulic cylinders with connecting pieces, as shown in Figure 3a. At the bottom of the confined water chamber, 34 drainage holes with a 10 mm diameter are equally distributed. In order to improve the sealing performance of the testing chamber, an installation conduit with a depth of 10 mm and a width of 25 mm is used to install the seal ring. The confined water chamber can also be used as the loading head, providing a vertical load to the testing material in the testing chamber. In order to improve the anti-deformation ability of the confined water chamber, the bottom of the confined water chamber is made

of a 20 mm thick stainless-steel plate with high strength, and a load-bearing frame is also added inside the chamber.

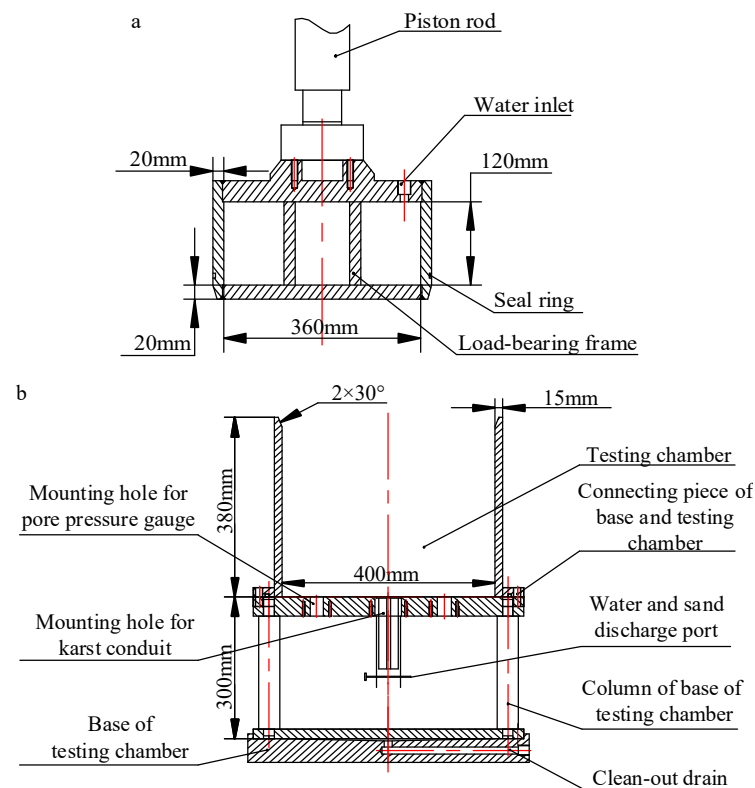


**Figure 3.** Structure of the confined water chamber and testing chamber: (a) confined water chamber; (b) testing chamber.

### (3) Testing chamber

The testing chamber is cylindrical, with an effective diameter of 400 mm and a height of 380 mm, as shown in Figure 3b. The testing chamber is connected to the base with a connecting piece with a circular seal ring. A water–sand inrush port that connects the testing chamber and the outside world is fixed to the base. Since each test requires the disassembly of the heavy testing chamber, it is difficult to ensure that the testing chamber is located in the center of the loading head during reinstallation, and the loading head and the testing chamber can easily sustain serious wear. Therefore, the base of the testing chamber is not fixed; instead, it is directly placed on the base of the testing system. The top of the testing chamber is chamfered. When the loading head enters the testing chamber, the position of the base of the testing chamber can be adjusted using the slight extrusion contact force between the loading head and the inner wall of the testing chamber, so as to align the loading head and the testing chamber.

### (4) Base of the testing chamber

The base of the testing chamber is shown in Figure 4. A mounting hole for a karst conduit with a diameter of 50 mm is placed in the center of the base of the testing chamber; it is used to place karst conduits of different sizes. Steel tubes with different inner diameters are used to simulate karst conduits with different sizes. A butterfly valve is installed at the bottom of the karst conduit as the device for instantaneously opening the karst conduit, which can simulate the initial moment of water–sand inrush through a karst conduit uncovered through tunnel excavation. Four mounting holes for the pore pressure gauges are distributed from the center to the edge of the base of the testing chamber; these gauges are used to monitor the distribution of the water pressure. The four pore pressure gauges



distributed from the center to the edge of the base of the testing chamber are numbered 1, 2, 3, and 4.

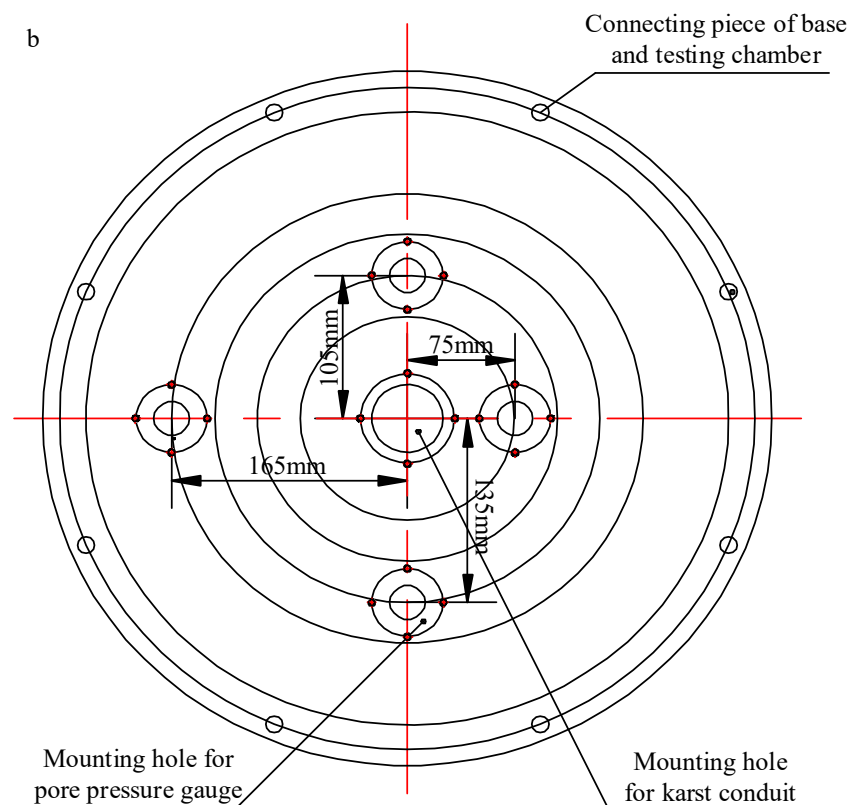
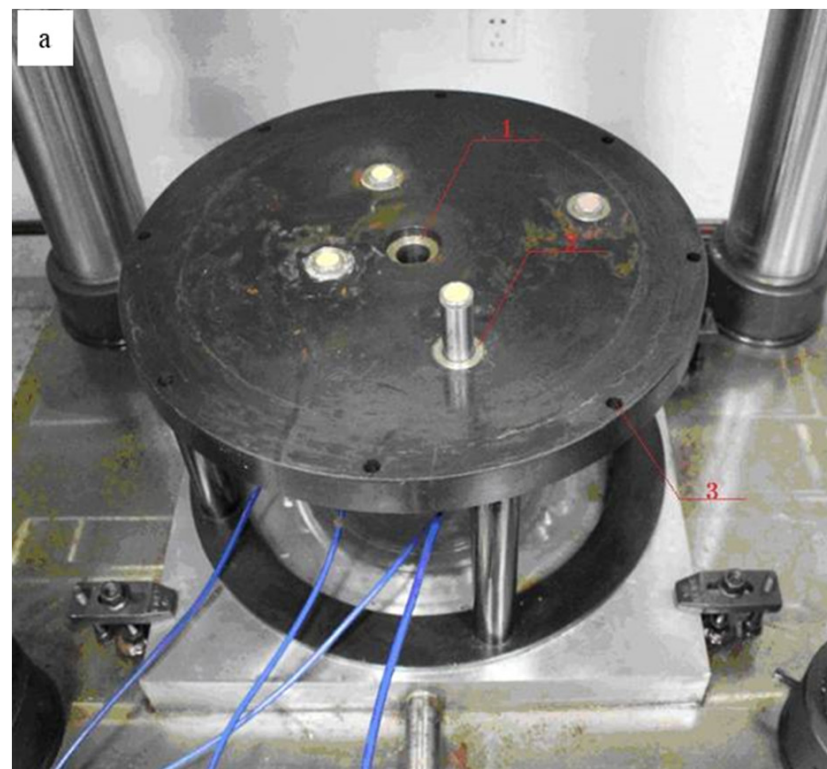


Figure 4. Cont.





**Figure 4.** Base of the testing chamber: (a) picture of the testing chamber; (b) structural plan of the testing chamber; (c) karst conduits of different sizes; (d) instantaneous opening device for the karst conduit.

#### (5) Storage tank

In order to guarantee the stability of the water pressure and water yield, we designed a storage tank. The storage tank is cylindrical, and its thickness, internal diameter, and height are 10 mm, 300 mm, and 1000 mm, respectively. The flowmeter and water pressure sensor are installed in the water outlet of the storage tank, which is located at the back of the storage tank.

#### (6) Control system

The control system consists of a console and a servo control system. The servo control system comprises a servo control system for the water pressure and water yield, and a servo control system for displacement and stress. (1) The console is fully automated, and five

basic parameters can be input into a database in real time; these include time, displacement, loading, water pressure, and water yield. The maximum sampling frequency is 10 Hz. (2) The servo control system for the water pressure and water yield can fill the testing chamber with water by setting the water pressure or water yield. The maximum water pressure is 2.0 MPa, the maximum water supply is 150 L/h, and the accuracy is 0.01 MPa. (3) The servo control system for displacement and loading can control the loading head by setting the displacement or load. The full scale of displacement of the meter is 400 mm, and the accuracy is 0.01 mm. The maximum load is 600 KN, and the accuracy is 0.01 KN.

### 3.2. Testing Scheme

The testing scheme of water–sand inrush included the following steps:

- (1) During water–sand inrush, the solid material is mainly silt sand and fine sand. Considering that the ratio of solid material is complex and varies from region to region, the scheme design did not deliberately aim to adopt a specific ratio. Clean river sand with a particle size of less than 0.3 mm was selected as the testing material, and a karst conduit with a diameter of 5 mm was placed in the mounting hole of the karst conduit.
- (2) The pore pressure gauges were installed in the corresponding mounting holes. In order to ensure the tightness of the testing chamber under the water pressure, a circle of sealant was applied at the ends of the pore pressure gauges during installation, and the pore pressure gauges were connected to the data acquisition system.
- (3) The testing chamber was placed on the base, and a sealing ring was placed between the base and the testing chamber. The instantaneous opening device for the karst conduit was closed. The river sand was packed into the testing chamber up to the designated height, i.e., 200 mm. The voidage of the river sand was 0.41.
- (4) Water was injected into the testing chamber until the total height of the water–sand mixture was 350 mm. As is known, the water–sand ratio is the volumetric ratio of water and sand in a water–sand mixture; therefore, the initial water–sand ratio for the water–sand inrush testing was 1.966. The testing system was initiated, the air vent on the upper part of the confined water chamber was opened, and a displacement control mode was adopted for the testing system to lower the confined water chamber to the position where it was essentially in contact with the water’s surface in the testing chamber, and to keep the displacement constant.
- (5) The air vent on the upper part of the confined water chamber was closed. The water pressure control mode was adopted for the testing system in order to increase the water pressure in the testing chamber to the initial design pressure of 0.1 Mpa, as shown in Figure 5. It is worth noting that the maximum flow rate that can be provided by the hydraulic water control system is 41 mL/s. Therefore, if the flow rate of the water–sand mixture reaches this value, the testing can be stopped.
- (6) After the above steps were carried out, the servo control system for the water pressure and water yield was closed, and the air vent on the upper part of the confined water chamber was opened again. The confined water chamber was slowly lifted to separate it from the testing chamber. After the whole testing system was cleaned, a karst conduit with a 6 mm diameter was placed in the mounting hole of the karst conduit, and then steps 1~5 were repeated until all of the karst conduits, with diameters ranging from 5 mm to 8 mm, had been tested.

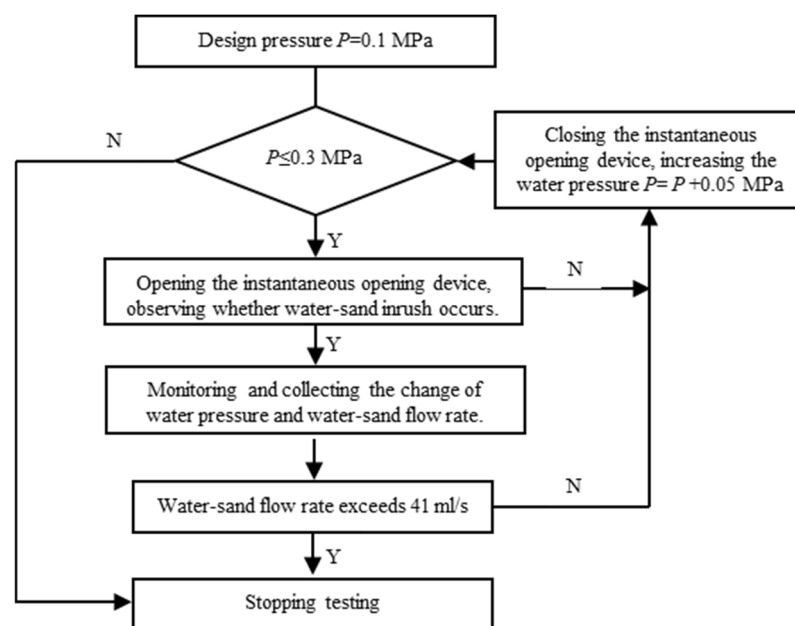


Figure 5. Flow chart of water-sand inrush testing.

#### 4. Testing Results and Analysis

##### 4.1. Change in Water-Sand Flow

With different set values of the water pressure, the relationships of the flow value and water pressure with time for the karst conduit with a diameter of 5 mm are shown in Figure 6.

Figure 6a shows the set value of the water pressure in the testing chamber to be 0.10 MPa. In the initial stage, the water-sand flow increased sharply, and it reached its maximum value of 19 mL/s at only 44 s. After maintaining the maximum value for about 30 s, the water-sand flow decreased sharply to 6.6 mL/s; it then dropped to about 6.0 mL/s after a sharp fluctuation (the peak value was 14 mL/s). After maintaining the value of 6.0 mL/s for about 50 s, another sharp fluctuation (the peak value was 15.8 mL/s) occurred. The overall trend was downward, and the value of the water-sand flow became zero after 315 s. The whole process of water-sand inrush can be summarized as follows: instability—migration—deposition—stability. When the instantaneous opening device was opened, there was no water-sand mixture in the karst conduit. Without considering the deformation of the karst conduit, the water-sand flow was at its highest at this time. However, with the movement of the water-sand mixture, the value of the water-sand flow was in a state of dynamic fluctuation, but the overall trend was downward. There are two main reasons for this: (1) In the initial stage of the water-sand movement, the karst conduit is gradually filled with the water-sand mixture, and the flow decreases due to the gradual increase in water-sand resistance. (2) During the water-sand movement, the water-sand mixture forms a stable arch structure, which prevents water-sand inrush. Therefore, the water pressure of 0.1 MPa can be defined as the critical head pressure of water-sand inrush when the height of the sand body is 200 mm and the aperture diameter of the karst conduit is 5 mm. It should be noted that the water pressure was not absolutely stable during water-sand inrush but fluctuated around 0.1 MPa. In the initial formation stage of the conduit, when the water-sand flow increased sharply, the water pressure was evidently lower than 0.1 MPa; this lasted for about 20 s.

The change in the water-sand flow when the set value of the water pressure was 0.15 MPa, 0.20 MPa, 0.25 MPa, and 0.30 MPa is shown in Figure 6b–e, respectively. When the karst conduit was opened suddenly, the actual water pressure in the testing chamber decreased significantly, due to the water-sand mixture flowing out of the testing chamber and the water supply lagging behind. With the stabilization of the water-sand flow, the

actual water pressure tended to gradually become stable, but it was still lower than the initial set water pressure. The actual values of the water pressure were 0.13 MPa, 0.18 MPa, 0.22 MPa, and 0.27 MPa. Therefore, the actual water pressure was chosen as the calculation basis. For the karst conduit with a diameter of 5 mm, the water–sand flow increased first and then stabilized over time under the action of the water pressure. With the increase in the set value of the water pressure, the steady flow of the water–sand mixture increased gradually. The steady flow values of the water–sand mixture under the action of the actual water pressures of 0.13 MPa, 0.18 MPa, 0.22 MPa, and 0.27 MPa were 8 mL/s, 17 mL/s, 20 mL/s, and 36 mL/s, respectively.

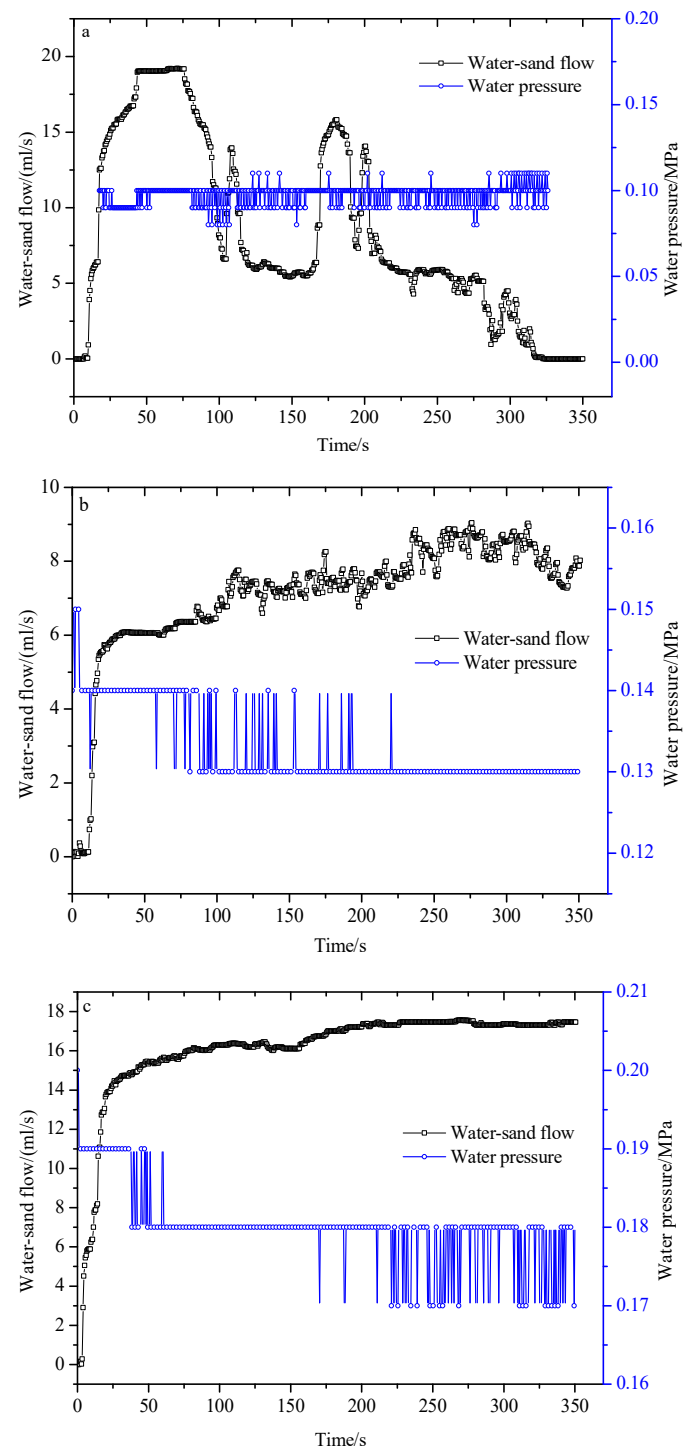
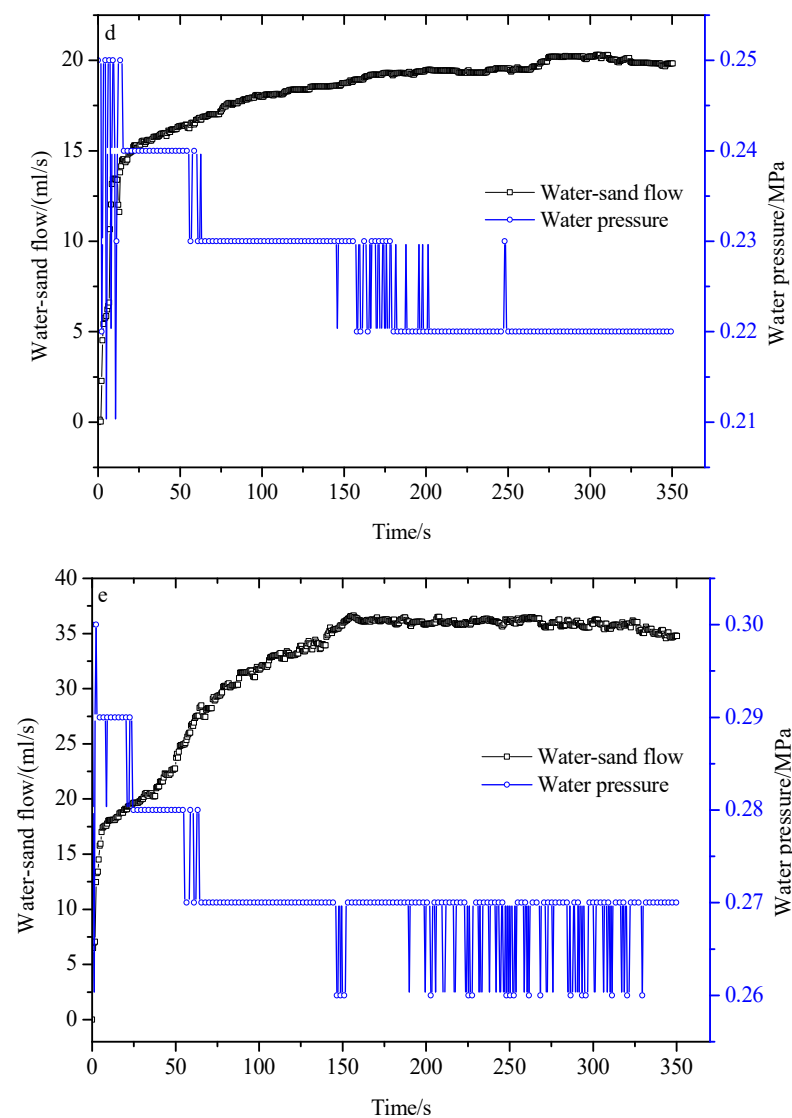


Figure 6. Cont.



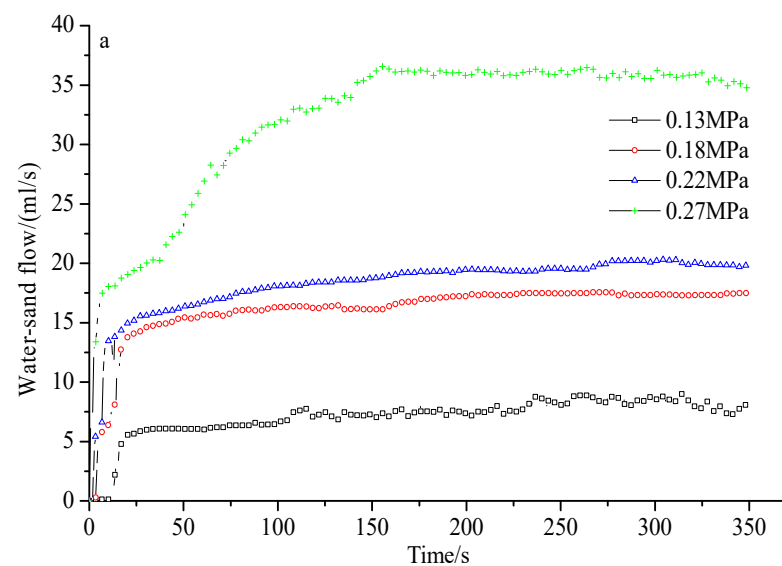
**Figure 6.** Relationships of the flow value and water pressure with time under different set values of the water pressure: (a) 0.10 MPa; (b) 0.15 MPa; (c) 0.20 MPa; (d) 0.25 MPa; (e) 0.30 MPa.

For the karst conduits with diameters ranging from 6 mm to 8 mm, when the set value of the water pressure in the testing chamber was high, the flow rate of the water–sand mixture rapidly exceeded the maximum flow rate (41 mL/s) that can be provided by the hydraulic water control system after the instantaneous opening device is opened; testing had to be stopped in this case. Along with the increase in the karst conduit’s diameter, the maximum water pressure required for the flow rate of the water–sand mixture to exceed the maximum flow rate (41 mL/s) gradually decreased. For the karst conduit that was 8 mm in diameter, when the set value of the water pressure in the testing chamber was greater than 0.10 MPa, the flow rate of the water–sand mixture rapidly exceeded the maximum flow rate. Moreover, the change trends of the flow value and water pressure with time for the karst conduits with diameters ranging from 5 mm to 8 mm were basically the same, except for the values. As such, the relationships of the flow value and water pressure with time for the karst conduits with diameters ranging from 6 mm to 8 mm are not displayed in figures, but are shown in Table 1.

**Table 1.** Change in the water–sand flow under different set values of the water pressure.

Diameter of Karst Conduit/mm	Set Value of Water Pressure/MPa	Actual Value of Water Pressure/MPa	Flow Rate of Water–Sand Mixture/(mL/s)
5	0.10	0.10	-
	0.15	0.13	8.0
	0.20	0.18	17.0
	0.25	0.22	20.0
	0.30	0.27	36.0
6	0.10	0.10	6.7
	0.15	0.13	16.7
	0.20	0.18	22.5
	0.25	0.22	40.5
	0.30	-	-
7	0.10	0.10	9.3
	0.15	0.12	19.0
	0.20	-	39.0
	0.25	-	-
	0.30	-	-
8	0.10	0.09	19.1
	0.15	-	-
	0.20	-	-
	0.25	-	-
	0.30	-	-

The relationship of the flow value with time for the karst conduits with diameters ranging from 5 mm to 8 mm is shown in Figure 7. The fitting relationships of the actual water pressure and the flow value when the flow value was stable are shown in Figure 8.

**Figure 7.** Cont.



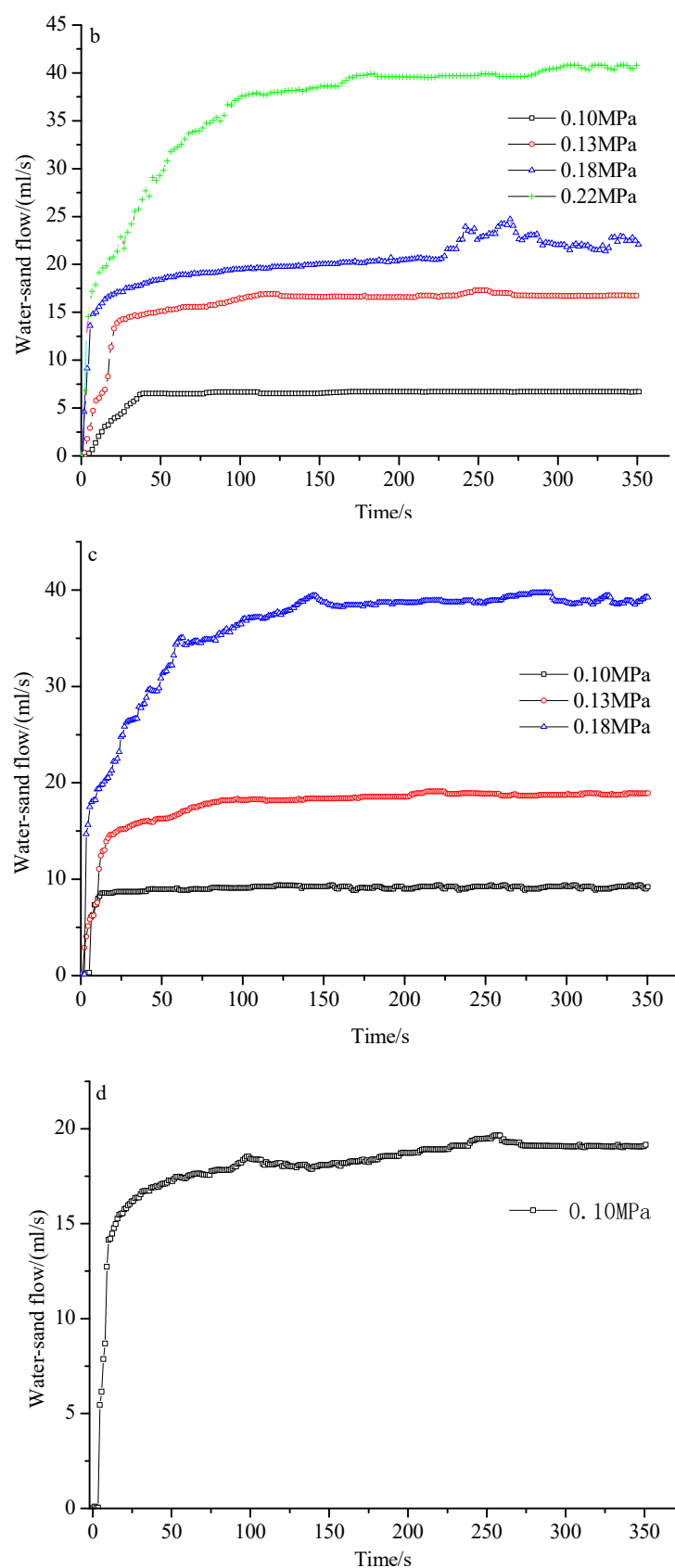


**Figure 7.** Relationship between the water pressure and flow value: (a) karst conduit with a 5 mm diameter; (b) karst conduit with a 6 mm diameter; (c) karst conduit with a 7 mm diameter; (d) karst conduit with an 8 mm diameter.

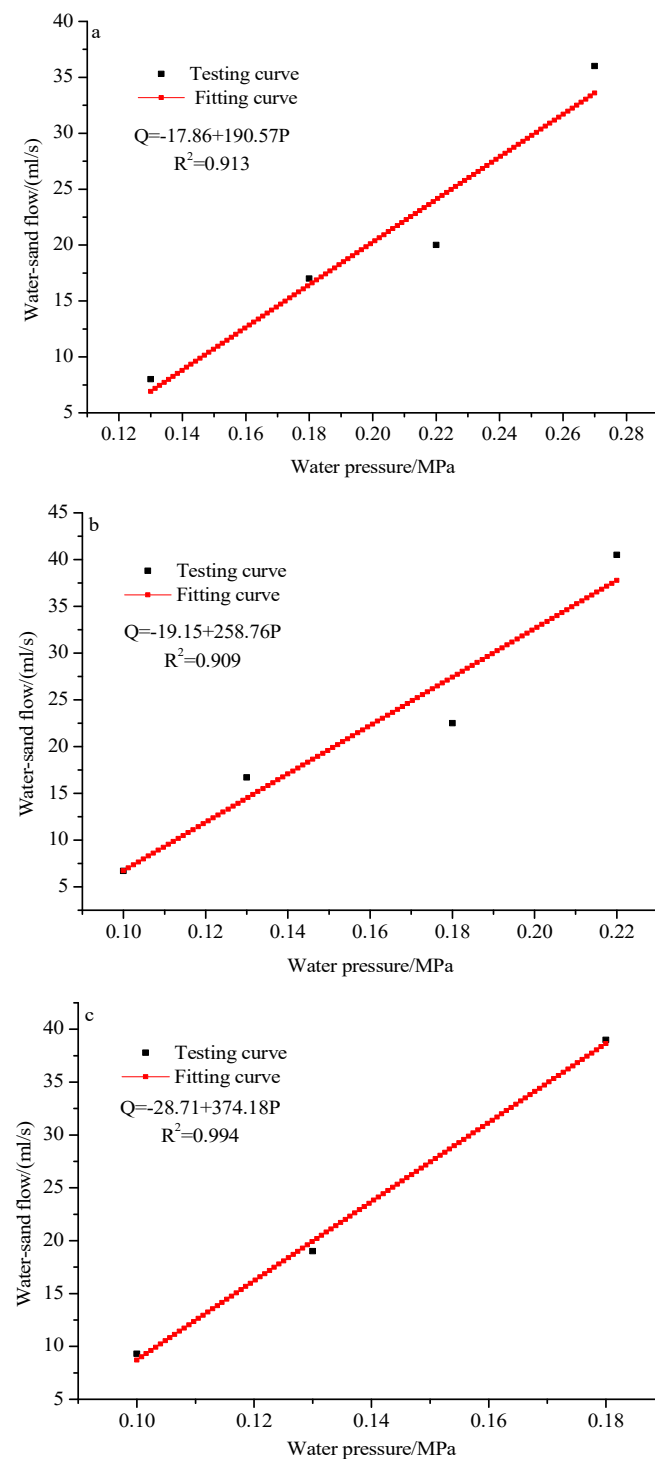


**Figure 8.** Fitting relationships between the actual water pressure and flow value: (a) karst conduit with a 5 mm diameter; (b) karst conduit with a 6 mm diameter; (c) karst conduit with a 7 mm diameter.

#### 4.2. Distribution of the Water Pressure near the Karst Conduit

For the karst conduit with a diameter of 5 mm, the distribution of the water pressure near the karst conduit is shown in Figure 9. The change trends of the water pressure near the karst conduits with diameters ranging from 5 to 8 mm were basically the same, except for the values. Therefore, the distribution of the water pressure near the karst conduits with diameters ranging from 6 to 8 mm are also not presented as figures; instead, they are presented in Table 2. When the karst conduit was opened, the values of the water pressure

monitored by the pore pressure gauges all clearly decreased. With the stabilization of the water–sand flow, the water pressure gradually became stable. With the increase in the distance between the pore pressure sensor and the karst conduit, the values of the water pressure all increased gradually, as shown in Figure 10.

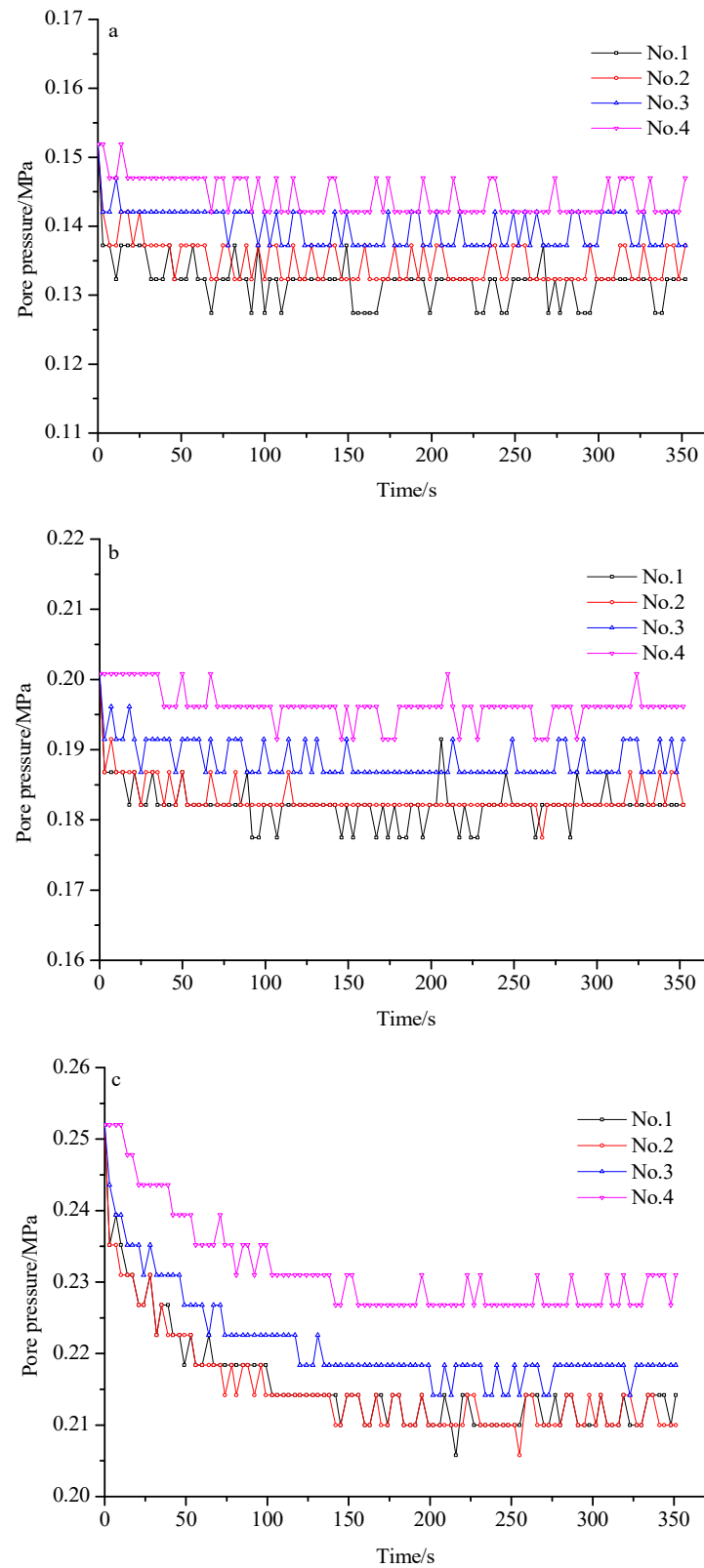
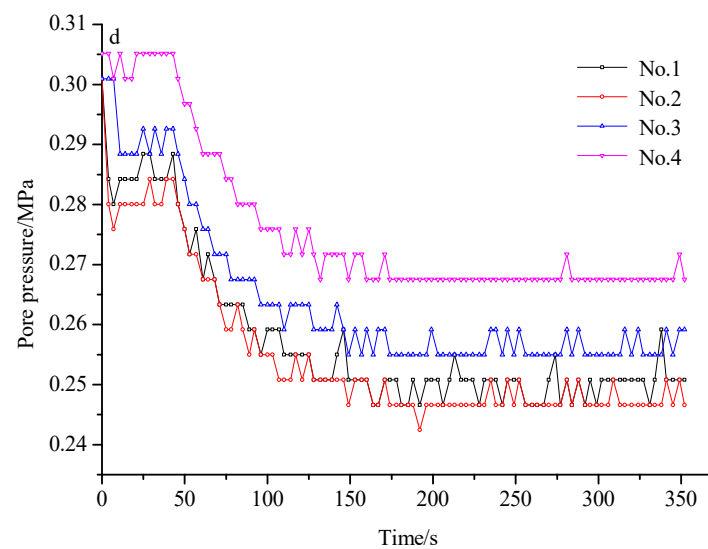


Figure 9. Cont.



**Figure 9.** Distribution of the water pressure near the karst conduit under different set values of the water pressure: (a) 0.15 MPa; (b) 0.20 MPa; (c) 0.25 MPa; (d) 0.30 MPa.

**Table 2.** Changes in the water pressure monitored by the pore pressure gauges.

Diameter of Karst Conduit/mm	Set Value of Water Pressure/MPa	Water Pressure Monitored by the Pore Pressure Gauges/MPa			
		No. 1	No. 2	No. 3	No. 4
5	0.10	-	-	-	-
	0.15	0.1323	0.1323	0.1372	0.1421
	0.20	0.1821	0.1821	0.1868	0.1961
	0.25	0.2100	0.2142	0.2184	0.2268
	0.30	0.2467	0.2508	0.2550	0.2675
6	0.10	0.0884	0.0884	0.0884	0.0942
	0.15	0.1345	0.1397	0.1448	0.1500
	0.20	0.1806	0.1806	0.1854	0.1903
	0.25	0.2107	0.2152	0.2198	0.2244
	0.30	-	-	-	-
7	0.10	0.0820	0.0860	0.0900	0.0940
	0.15	0.1288	0.1344	0.1344	0.1400
	0.20	0.1684	0.1729	0.1775	0.1820
	0.25	-	-	-	-
	0.30	-	-	-	-
8	0.10	0.0778	0.0834	0.0890	0.0945
	0.15	-	-	-	-
	0.20	-	-	-	-
	0.25	-	-	-	-
	0.30	-	-	-	-

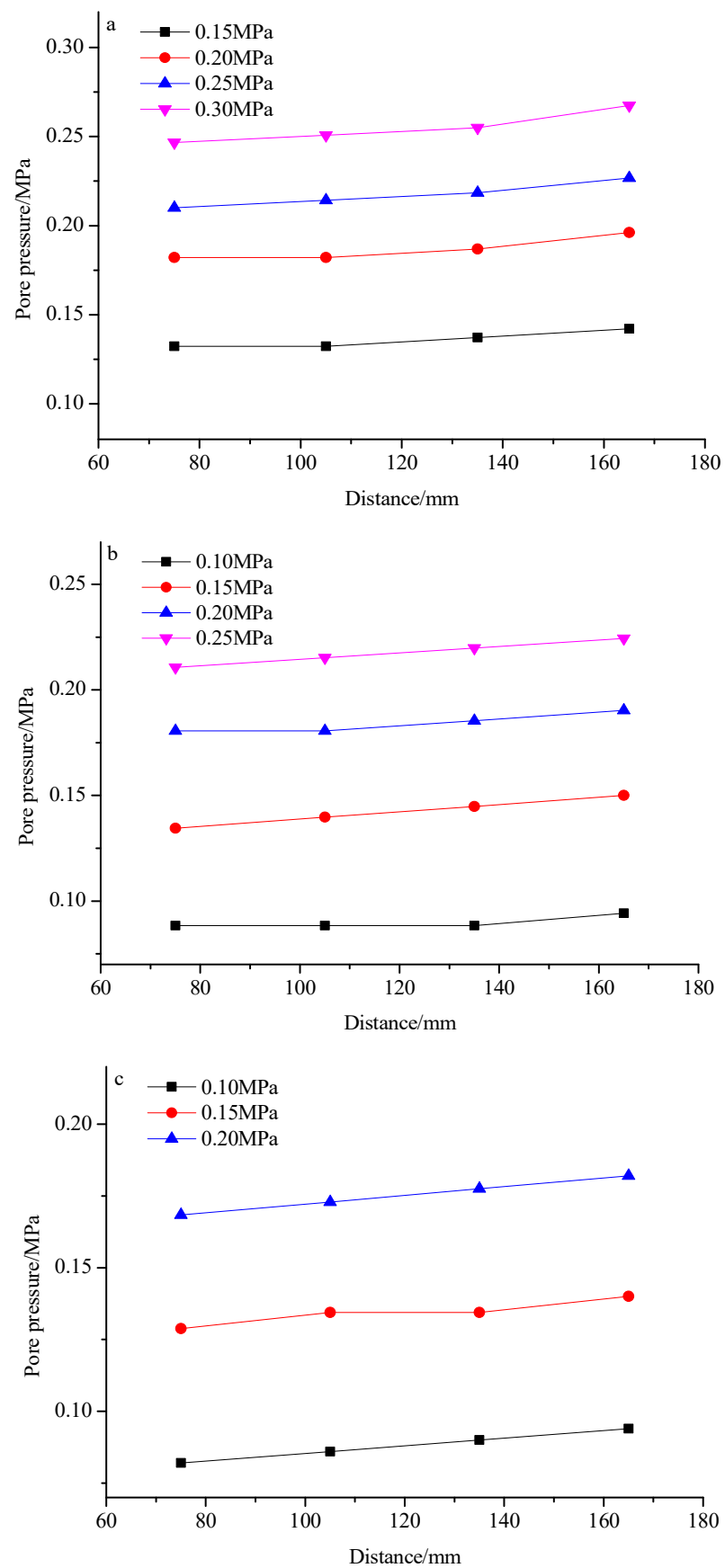
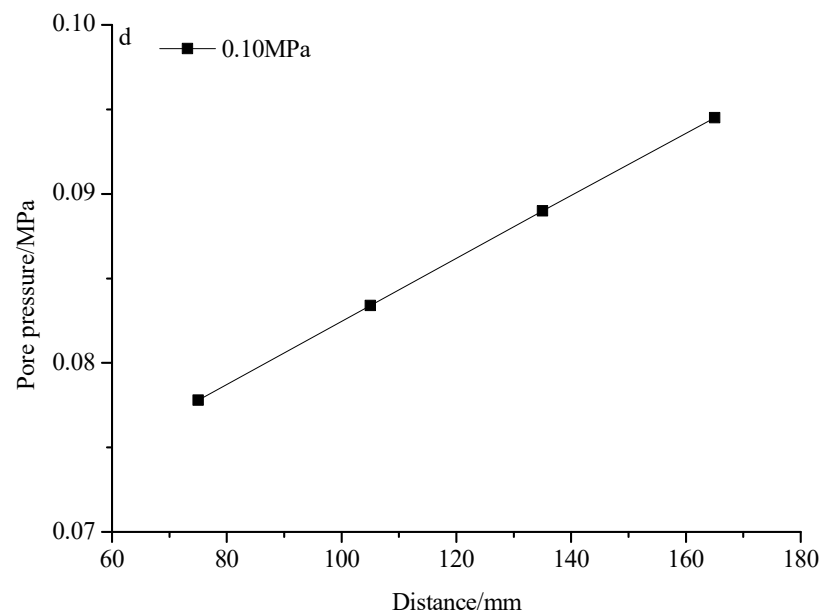


Figure 10. Cont.



**Figure 10.** Changes in the pore pressure as the distance between the pore pressure sensor and the karst conduit increased: (a) karst conduit with a 5 mm diameter; (b) karst conduit with a 6 mm diameter; (c) karst conduit with a 7 mm diameter; (d) karst conduit with an 8 mm diameter.

## 5. Conclusions

- (1) The process of water–sand inrush through a karst conduit is akin to a water–sand mixture flowing through the discharge opening of a storage bin. Based on force analysis of a non-aqueous sand body above a karst conduit, the limit width of the karst conduit under force equilibrium was obtained. Considering the effect of water on aqueous sand bodies, the criterion of water–sand inrush was established.
- (2) The simulated testing system for water–sand inrush through karst conduits consisted of a loading support bracket, a confined water chamber (loading head), a testing chamber, the base of the testing chamber, a storage tank, a servo control system for the water pressure and water yield, a servo control system for displacement and stress, and a console. Moreover, the steps for testing water–sand inrush were also designed.
- (3) When the water pressure in the testing chamber was close to the critical head pressure of the water–sand inrush, the water–sand inrush exhibited the pattern of instability—migration—deposition—stability. When the water pressure in the testing chamber exceeded the critical head pressure, the water–sand flow first increased and then stabilized over time. With the increase in the set values of the water pressure and conduit size, the steady flow of the water–sand mixture increased gradually. When the karst conduit was opened suddenly, the actual water pressure in the testing chamber decreased significantly, due to the water–sand mixture flowing out of the testing chamber and the water supply lagging behind. With the stabilization of the water–sand flow, the actual water pressure gradually tended towards stability, but it was still lower than the water pressure that was initially set.
- (4) When the karst conduit was opened, the water pressure values monitored by the pore pressure gauges all clearly decreased. With the stabilization of the water–sand flow, the water pressure gradually became stable. With the increase in the distance between the pore pressure sensor and the karst conduit, the water pressure values all increased gradually. The results of this test are significant in relation to the further study of the formation mechanisms of water–sand inrush through karst conduits.



**Author Contributions:** Conceptualization, H.W.; methodology, H.W. and Z.Z. (Zhenhua Zhao); formal analysis, Z.Z. (Zhenhua Zhao) and L.H.; investigation, L.H. and Z.Z. (Zhenlong Zhao); writing—original draft preparation, Z.Z. (Zhenhua Zhao); writing—review and editing, Z.Z. (Zhenhua Zhao), H.W., L.H. and Z.Z. (Zhenlong Zhao); supervision, Z.Z. (Zhenhua Zhao) and H.W.; funding acquisition, H.W. All authors have read and agreed to the published version of the manuscript.

**Funding:** This work was funded by the Youth Innovation Team Plan of Colleges and Universities in Shandong Province (2022KJ112), the China Postdoctoral Science Foundation (2022M711969), the National Natural Science Foundation of China (51704152), and the Natural Science Foundation of Shandong Province (ZR2017BEE001).

**Data Availability Statement:** Not applicable.

**Conflicts of Interest:** The authors declare no conflict of interest.

## References

1. Parise, M.; Closson, D.; Gutiérrez, F.; Stevanović, Z. Anticipating and managing engineering problems in the complex karst environment. *Environ. Earth Sci.* **2015**, *74*, 7823–7835. [\[CrossRef\]](#)
2. Zhang, K.; Zhang, W.B.; Liao, Z.Y.; Xie, H.P.; Zhou, C.T.; Chen, S.G.; Zhu, J.B. Risk assessment of ground collapse along tunnels in karst terrain by using an improved extension evaluation method. *Tunn. Undergr. Space Technol.* **2022**, *129*, 104669. [\[CrossRef\]](#)
3. Waele, D.J.; Gutiérrez, F.; Parise, M.; Plan, L. Geomorphology and natural hazards in karst areas: A review. *Geomorphology* **2011**, *124*, 1–8. [\[CrossRef\]](#)
4. Cui, Q.L.; Wu, H.N.; Shen, S.L.; Xu, Y.S.; Ye, G.L. Chinese karst geology and measures to prevent geohazards during shield tunnelling in karst region with caves. *Nat. Hazards* **2015**, *77*, 129–152. [\[CrossRef\]](#)
5. Fan, H.B.; Zhang, Y.H.; He, S.Y.; Wang, K.; Wang, X.L.; Wang, H. Hazards and treatment of karst tunneling in Qinling-Daba mountainous area: Overview and lessons learnt from Yichang-Wanzhou railway system. *Environ. Earth Sci.* **2018**, *77*, 679–696. [\[CrossRef\]](#)
6. Xue, F.; Cai, M.J.; Wang, T.Z.; Zhao, T.Y. Characteristics of karst cave development in urban karst area and its effect on the stability of subway tunnel construction. *Adv. Civ. Eng.* **2021**, *2021*, 8894713. [\[CrossRef\]](#)
7. Li, S.C.; Lin, P.; Xu, Z.H.; Li, L.P.; Guo, M.; Sun, C.Q.; Wang, J.; Song, S.G. Minimum safety thickness of water and mud inrush induced by filled-type karst water bearing structures based on theory of slice method. *Rock Soil Mech.* **2015**, *36*, 1989–1994. [\[CrossRef\]](#)
8. Wang, J.X.; Feng, B.; Zhang, X.S.; Tang, Y.Q.; Yang, P. Hydraulic failure mechanism of karst tunnel surrounding rock. *Chin. J. Rock Mech. Eng.* **2010**, *29*, 1363–1370.
9. Zhang, K.; Tannant, D.D.; Zheng, W.B.; Chen, S.G.; Tan, X.R. Prediction of karst for tunnelling using fuzzy assessment combined with geological investigations. *Tunn. Undergr. Space Technol.* **2018**, *80*, 64–77. [\[CrossRef\]](#)
10. Alija, S.; Torrijo, F.J.; Quinta-Ferreira, M. Geological engineering problems associated with tunnel construction in karst rock masses: The case of Gavarres tunnel (Spain). *Eng. Geol.* **2013**, *157*, 103–111. [\[CrossRef\]](#)
11. Zini, L.; Chiara, C.; Franco, C. The challenge of tunneling through Mediterranean karst aquifers: The case study of Trieste (Italy). *Environ. Earth Sci.* **2015**, *74*, 281–295. [\[CrossRef\]](#)
12. Zheng, Y.C.; He, S.Y.; Yu, Y.; Zheng, J.Y.; Zhu, Y.; Liu, T. Characteristics, challenges and countermeasures of giant karst cave: A case study of Yujingshan tunnel in high-speed railway. *Tunn. Undergr. Space Technol.* **2021**, *114*, 103988. [\[CrossRef\]](#)
13. Huang, X.; Li, S.C.; Xu, Z.H.; Guo, M.; Shi, X.S.; Gao, B.; Zhang, B.; Liu, L. An attribute recognition model for safe thickness assessment between concealed karst cave and tunnel. *J. Cent. South Univ.* **2019**, *26*, 955–969. [\[CrossRef\]](#)
14. Kaufmann, G.; Romanov, D. Modelling long-term and short-term evolution of karst in vicinity of tunnels. *J. Hydrol.* **2020**, *581*, 124282. [\[CrossRef\]](#)
15. Lv, Y.X.; Jiang, Y.J.; Hu, W.; Cao, M.; Mao, Y. A review of the effects of tunnel excavation on the hydrology, ecology, and environment in karst areas: Current status, challenges, and perspectives. *J. Hydrol.* **2020**, *586*, 124891. [\[CrossRef\]](#)
16. Li, S.C.; Pan, D.D.; Xu, Z.H.; Li, L.L.; Lin, P.; Yuan, Y.C.; Gao, C.L.; Lu, W. A model test on catastrophic evolution process of water inrush of a concealed karst caved filled with confined water. *Rock Soil Mech.* **2018**, *39*, 3164–3173. [\[CrossRef\]](#)
17. Wang, X.T.; Li, S.C.; Xu, Z.H.; Hu, J.; Pan, D.D.; Xue, Y.G. Risk assessment of water inrush in karst tunnels excavation based on normal cloud model. *Bull. Eng. Geol. Environ.* **2019**, *78*, 3783–3798. [\[CrossRef\]](#)
18. Li, S.C.; Wang, K.; Li, L.L.; Zhou, Z.Q.; Shi, S.S.; Liu, S. Mechanical mechanism and development trend of water-inrush disasters in karst tunnels. *Chin. J. Theor. Appl. Mech.* **2017**, *49*, 22–30.
19. Liu, Q.; Chen, W.Z.; Yuan, J.Q.; Wang, Y.X.; Wan, H. Evaluation of grouting reinforcement effect for karst filling medium based on seepage-erosion theory. *Chin. J. Rock Mech. Eng.* **2020**, *39*, 572–580. [\[CrossRef\]](#)
20. Casagrande, G.; Cucchi, F.; Zini, L. Hazard connected to railway tunnel construction in karstic area: Applied geomorphological and hydrogeological surveys. *Nat. Hazards Earth Syst. Sci.* **2005**, *5*, 243–250. [\[CrossRef\]](#)
21. Wang, J.; Li, S.C.; Li, L.P.; Lin, P.; Xu, Z.H.; Gao, C.L. Attribute recognition model for risk assessment of water inrush. *Bull. Eng. Geol. Environ.* **2019**, *78*, 1057–1071. [\[CrossRef\]](#)

22. Kang, Y.; Yang, C.H.; Zhang, P. Disaster-induced mechanism and its treatment in shallow-buried karst tunnel. *Chin. J. Rock Mech. Eng.* **2010**, *29*, 149–154.
23. Li, S.C.; Xu, Z.H.; Huang, X.; Lin, P.; Zhao, X.C.; Zhang, Q.S.; Yang, L.; Zhang, X.; Sun, H.F.; Pan, D.D. Classification, geological identification, hazard mode and typical case studies of hazard-causing structures for water and mud inrush in tunnels. *Chin. J. Rock Mech. Eng.* **2018**, *37*, 1041–1069. [[CrossRef](#)]
24. Xu, Z.H.; Lin, P.; Xing, H.L.; Pan, D.D.; Huang, X. Hydro-mechanical coupling response behaviors in tunnel subjected to a water-filled karst cave. *Rock Mech. Rock Eng.* **2021**, *54*, 3737–3756. [[CrossRef](#)]
25. Zhang, W.S.; Jiao, Y.Y.; Zhang, G.H.; Zhang, X.; Ou, G.Z.; Lin, Z.P. Analysis of the mechanism of water inrush geohazards in deep-buried tunnels under the complex geological environment of karst cave-fractured zone. *J. Earth Sci.* **2022**, *33*, 1204–1218. [[CrossRef](#)]
26. Zhou, Y.; Li, S.C.; Li, L.P.; Zhang, Q.Q.; Shi, S.S.; Song, S.G.; Wang, K.; Chen, D.Y.; Sun, S.Q. New technology for fluid-solid coupling tests of underground engineering application in experimental simulation of water inrush in filled-type karst and its conduit. *Chin. J. Geotech. Eng.* **2015**, *37*, 1232–1240. [[CrossRef](#)]
27. Pan, D.D.; Li, S.C.; Xu, Z.H.; Li, L.L.; Lu, W.; Lin, P.; Huang, X.; Sun, S.Q.; Gao, C.L. Model tests and numerical analysis for water inrush caused by karst caves filled with confined water in tunnels. *Chin. J. Geotech. Eng.* **2018**, *40*, 828–836. [[CrossRef](#)]
28. Wang, H.L.; Chen, S.J.; Guo, W.J. Development and application of test system for water-sand inrush. *J. Min. Saf. Eng.* **2019**, *36*, 72–79. [[CrossRef](#)]
29. Zhou, Y.; Li, S.C.; Li, L.P.; Shi, S.S.; Zhang, Q.Q.; Chen, D.Y.; Song, S.G. 3D Fluid-solid coupled model test on water-inrush in tunnel due to seepage from filled karst conduit. *Chin. J. Rock Mech. Eng.* **2015**, *34*, 1739–1749. [[CrossRef](#)]
30. Chu, V. Mechanism numerical on water inrush disaster of filling karst piping and analysis of evolutionary process in highway tunnel. *J. Cent. South Univ.* **2016**, *47*, 4173–4180. [[CrossRef](#)]
31. Huang, Z.; Zeng, W.; Li, X.Z.; Zhang, P.X.; Wu, Y.; Zhao, K.; Li, S.J. Numerical analysis of fracture-induced water inrushes in karst underground engineering. *J. Basic Sci. Eng.* **2021**, *29*, 412–425. [[CrossRef](#)]
32. Li, L.P.; Li, S.C.; Zhang, Q.S. Study of mechanism of water inrush induced by hydraulic fracturing in karst tunnels. *Rock Soil Mech.* **2010**, *31*, 523–552. [[CrossRef](#)]
33. Liu, Z.W.; He, M.C.; Wang, S.R. Study on karst water burst mechanism and prevention countermeasures in Yuanliangshan tunnel. *Rock Soil Mech.* **2006**, *27*, 228–232. [[CrossRef](#)]
34. Li, S.C.; Gao, C.L.; Zhou, Z.Q.; Li, L.P.; Wang, M.X.; Yuan, Y.C.; Wang, J. Analysis on the precursor information of water inrush in karst tunnels: A true triaxial model test study. *Rock Mech. Rock Eng.* **2019**, *52*, 373–384. [[CrossRef](#)]
35. Zhu, W.S.; Zhang, Q.B.; Zhu, H.H.; Li, Y.; Yin, J.H.; Li, S.C.; Sun, L.F.; Zhang, L. Large-scale geomechanical model testing of an underground cavern group in a true three-dimensional (3-D) stress state. *Can. Geotech. J.* **2010**, *47*, 935–946. [[CrossRef](#)]

**Disclaimer/Publisher’s Note:** The statements, opinions and data contained in all publications are solely those of the individual author(s) and contributor(s) and not of MDPI and/or the editor(s). MDPI and/or the editor(s) disclaim responsibility for any injury to people or property resulting from any ideas, methods, instructions or products referred to in the content.